PAPER

Check for updates

How organic switches grafting on TiO_2 modifies the surface potentials: theoretical insights†

Haiming Huang, [ID] *[ab] Mingquan Ding,[ab] Yu Zhang,[ab] Shuai Zhang,[ab] Yiyun Ling, [ID] [a] Weiliang Wang [ID] *[c] and Shaolin Zhang [ID] *[ab]

Hybrid organic switch-inorganic semiconductor systems have important applications in both photo-responsive intelligent surfaces and microfluidic devices. In this context, herein, we performed first-principles calculations to investigate a series of organic switches of *trans/cis*-azobenzene fluoride and pristine/oxidized trimethoxysilane adsorbed on low-index anatase slabs. The trends in the surface–adsorbate interplay were examined in terms of the electronic structures and potential distributions. Consequently, it was found that the *cis*-azobenzene fluoride (oxidized trimethoxysilane)-terminated anatase surface attains a lower ionization potential than the *trans*-azobenzene fluoride (pristine trimethoxysilane)-terminated anatase surface due to its smaller induced (larger intrinsic) dipole moment, whose direction points inwards (outwards) from the substrate, which originates from the electron charge redistribution at the interface (polarity of attached hydroxyl groups). By combining the induced polar interaction analysis and the experimental measurements in the literature, we demonstrate that the ionization potential is an important predictor of the surface wetting properties of adsorbed systems. The anisotropic absorbance spectra of anatase grafted with azobenzene fluoride and trimethoxysilane are also related to the photoisomerization and oxidization process under UV irradiation, respectively.

1 Introduction

Reversible photochemical processes on photosensitive materials enable a switchable change in their surface properties, *e.g.*, wettability, adhesion and color, under the influence of external stimuli in an environmentally friendly, non-contact and convenient manner,[1–6] and thus have found significant applications in chemical sensors,[7] artificial intelligent surfaces,[5] and microfluidic devices.[3] One well-known strategy to obtain dynamically modifiable surface properties exploits the changes in geometry and dipole moment resulting from photochromism in surface-confined organic molecules, including azobenzene (AZB),[8,9] diarylethene (DTE),[10] spiropyran (SP)[11] and their derivatives. Another approach toward more pronounced and switchable property changes exploits the reversible property of some semiconductor oxides such as ZnO,[12–14] WO_3,[15] and TiO_2.[16–18] Recently, many studies, mainly from an experimental

viewpoint, have been directed toward combining organic switches with inorganic materials[19–21] given that the resulting hybrid systems are believed to be the key to expanding the applicability of the subsystems in realistic devices. The corresponding investigations include the study of the colorless-colored isomerization of SP derivatives on porous TiO_2,[22] *cis–trans* isomerization of azobenzene fluoride derivatives adsorbed on metal oxide nanoparticles,[23] and trimethoxy(alkyl)silane grafted on TiO_2 nanoparticles.[24,25] Moreover, artificial joint systems (*e.g.*, metal/ZnO, metal/insulator/semiconductor and bipyridine-complexes/TiO_2) have also been found to be a promising solution for integrated and efficient solar-to-chemical conversion,[26–30] indicating their potential applications in the field of energy utilization. These investigations confirm that immobilized organic switches and inorganic semiconductor oxide substrates may retain their photosensitive and modifiable properties in joint systems.[19,31,32]

In this case, a good understanding of hybrid systems is crucial to quantify the interplay between the organic switches and inorganic substrates during the photochemical process. To explore the optoelectronic properties of these hybrid systems, numerous studies have carried out, including density functional theory (DFT)/time-dependent density functional theory (TDDFT) investigation of a series of photochromic derivatives of *trans/cis*-AZB,[33] open/closed-SP[34] and open/closed-DTE[33,35] adsorbed onto anatase and rutile slabs. To explain the switchable wettability of TiO_2 nanoparticles modified with

[a]Solid State Physics & Material Research Laboratory, School of Physics and Materials Science, Guangzhou University, Guangzhou 510006, China. E-mail: huanghm@gzhu. edu.cn; slzhang@gzhu.edu.cn

[b]Research Center for Advanced Information Materials (CAIM), Huangpu Research and Graduate School of Guangzhou University, Guangzhou 510555, China

[c]School of Physics, Guangdong Province Key Laboratory of Display Material and Technology, Sun Yat-sen University, Guangzhou 510275, China. E-mail: wangwl2@ mail.sysu.edu.cn

† Electronic supplementary information (ESI) available. See DOI: https://doi.org/10.1039/d3ra00537b

Paper

trimethoxysilane under UV illumination, a series of experiments was carried out to confirm the oxidization process for the degradation of trimethoxysilane.[24,25] However, complementary computational efforts to model the surface of these systems and interface properties are lacking.

Surface potential is one of the basic physical characteristics of a material surface, which is related to its surface properties (through the Fermi energy), given that it can dictate the direction of charge transfer, and thereby significantly affect the stability and surface chemistry of surfaces with adsorbates.[36–38] Particularly, the work function (ionization potential) of the metallic (semiconducting or insulating) surface is one of the most important technological parameters of the surface potential[39,40] in developing new field-emitter cathodes or photo-responsive superhydrophobic surfaces for applications in light-emitting diodes and smart fluid control. By using the surface polarizability approach and performing contact angle measurements, the surface polarizability, which has been observed to exhibit a significant inverse relationship with respect to the ionization potential,[41–43] was found to be closely related to the surface free energy and wettability.[44] By combining first-principle calculation with contact angle measurement, the work function was demonstrated to be a critical quantity in understanding the wettability of silane coatings.[45] Based on first-principles density functional theory, low-dimensional materials with a low work function have been demonstrated to have a considerable impact on the power efficiency for field-emission applications.[46] However, a limited number of studies has been conducted on the surface potentials of joint systems that incorporate organic switches in inorganic surfaces. In this case, how the functional organic switch configuration, low-index semiconductor surface and surface–adsorbate interplay influence the electronic properties and surface potential barriers of the joint system remains an unsolved issue. Furthermore, the difference in surface potentials between a series of organic switches grafted on various inorganic semiconductor surfaces still needs to be studied in depth.

Herein, we used DFT to investigate the electronic properties and surface potentials of hybrid organic/inorganic systems with different organic adsorbates and various low-index TiO$_2$ surfaces. We show that the change in the ionization potential during the photoisomerization and oxidation processes of the organic switch configuration is correlated with the changes in the surface dipole moments. We demonstrate that the ionization potentials play an important role in determining the potential barriers, and consequently justify their surface-wetting properties. This work is organized as follows: the Computational methods section provides the physical model and the computational methodology. The results and their interpretations are presented in the Results and discussion section. Finally, the Conclusions section provides a general summary of this work.

2 Computational methods

To quantify the mutual influence between organic and inorganic subsystems, we performed a DFT study on two commonly used organic coatings, *i.e.*, azobenzene fluoride (FAZB) and 1*H*,1*H*,2*H*,2*H*-perfluorooctyl(trimethoxy)silane (PFOS), grafted on anatase TiO$_2$ surfaces modeled as a periodic slab, as shown in Fig. 1 and S1.† To ensure immobilization of the coating to the surface, the *trans*-FAZB and *cis*-FAZB isomers were anchored on surfaces with strong binding by adding carboxyl groups on one side of the isomer,[33,47] while the oxygen atom in the siloxane groups of PFOS binds to the surface the titanium atom.[45] We considered the perpendicular configuration of the organic switches adsorbed on anatase slabs given that the present work aimed to explore the changes in the polarity and surface potentials of immobilized organic switches in the perpendicular direction during the photoisomerization and photo-induced oxidation process, which proceeded *via* rotation or inversion mechanisms in sufficient space. The perpendicular configuration was also demonstrated to be the optimal adsorption mode in terms of energetic and dynamical stability.[30,47–50] The effectiveness of adding anchor groups was predicted through both experimental and theoretical studies,[34,47,49] while the covalent bonding of trimethoxysilane refers to a grafting reaction with silanes in the real synthesis process.[50,51] To consider the effect of the oxidization of PFOS due to UV illumination, one of the fluorine atoms at the end of the carbon chain of pristine PFOS (labeled as PFOS-F) was replaced by a hydroxyl group, which was labeled as PFOS-OH. Considering their widespread use as photoelectrode substrates, we selected two types of commonly used stable anatase TiO$_2$ faces, *i.e.*, (100) and (101), as the inorganic surfaces.[52] Particularly, there are two inequivalent anatase (101) surfaces (Fig. S1†), and thus for clarity, they will be referred to as (101)-I and (101)-II herein.
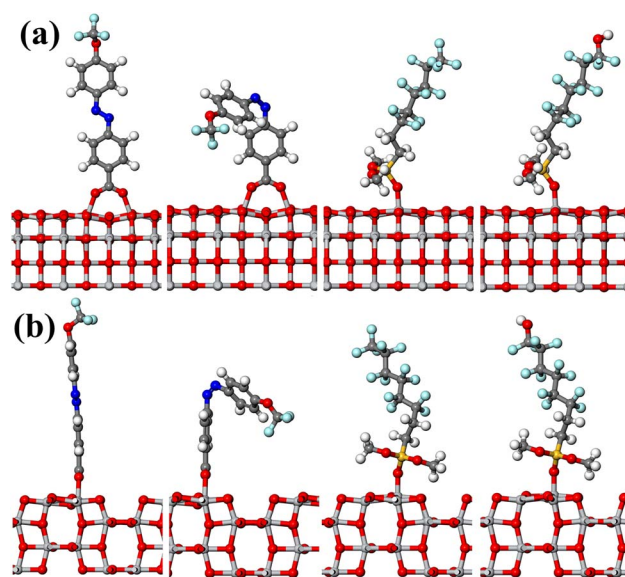

Fig. 1 Adsorbed structures of (left to right) *trans*-FAZB, *cis*-FAZB, PFOS-F and PFOS-OH on anatase TiO$_2$ (100) surface viewed along (a) *y*-axis and (b) *x*-axis. The white, gray, blue, red, gold, light-gray and light-blue spheres represent hydrogen, carbon, nitrogen, oxygen, silicon, titanium and fluorine atoms, respectively.

We carried out DFT calculations with the Perdew–Burke–Ernzerhof (PBE)[53] form of the generalized gradient approximation (GGA) for the exchange-correlation functional to optimize the atomic structures and calculate the electronic structures, as implemented in the Vienna *ab* initio simulation package (VASP).[54,55] The ion–electron interactions were treated using the projector augmented wave (PAW) method[56] with a cutoff energy of 400 eV. The two-dimensional joint system was modeled by using the supercell approximation with at least a 25 Å vacuum space along the direction perpendicular to the surface, which was taken to be the *z*-axis, to eliminate interactions between periodic images. From the bulk anatase cell, a four-layer 4×1 and 1×4 slab was cut in the (100) and (101) directions, presenting dimensions of 11.36×9.87 Å^2 and 10.57×11.36 Å^2 in the *x–y* plane, respectively, and the bottom layer along the *z* direction was fixed. All the selected atoms were fully relaxed using the conjugate gradient method until the magnitude of the force on each atom became less than 0.01 eV Å^{-1} in the optimized structures and the total energies were converged within 10^{-5} eV per cell. For the structural optimization (static calculations), the Brillouin zone was sampled using a set of $2 \times 2 \times 1$ $(4 \times 4 \times 1)$ Monkhorst–Pack *k* points.[57] The Gaussian smearing scheme was applied with a smearing width of 0.14 eV. The adsorption coverage in our calculation corresponded to one organic adsorbate per TiO$_2$ 4×1 (1×4) supercell for the (100) [(101)] surface, *i.e.*, $\sim 8.9 \times 10^{13}$ cm^{-2} ($\sim 8.3 \times 10^{13}$ cm^{-2}) for (100) [(101)] surface. The coverage we considered is in the reasonable range reported in previous experimental and theoretical studies.[48,49,58]

The ionization potential (work function) for a semiconductor (metal) was derived from the energy difference between the vacuum level and the valence band maximum (Fermi energy). Generally, the Fermi level is located between the conduction band minimum and the valence band maximum depending on the hybrid and surface states. Given that the adsorption is on only one side of the hybrid organic/inorganic surface, in the calculation of surface potentials, we put two joint systems with mirror symmetry in the supercell to create two vacuum regions with constant vacuum potentials to obtain two independent vacuum levels of the two sides of the surface. It is noteworthy that our computational approach was validated by performing sets of work function calculations on silane-modified substrates[45] and graphene edges.[37]

3   Results and discussion

We begin our discussion by focusing on the structures of the adsorbed systems. Examples of the relaxed atomic structures of FAZB and PFOS chemisorbed on the anatase (100) surface are shown in Fig. 1 [adsorption on anatase (101)-I and (101)-II surfaces is depicted in Fig. S1†]. To determine the stability of hybrid systems, we investigated the adsorption energies of organic/inorganic interfaces. The adsorption energy E_a of the organic switch can be expressed as $E_a = E_{hybrid} - (E_o + E_{ino})$, where E_{hybrid} is the total energy of the hybrid system with organic adsorbates, E_o is the energy of an isolated organic functional group, and E_{ino} is the energy of an inorganic

Table 1 Total energies and adsorption energies of 12 species of considered hybrid systems in comparison to inorganic group-grafted anatase surfaces

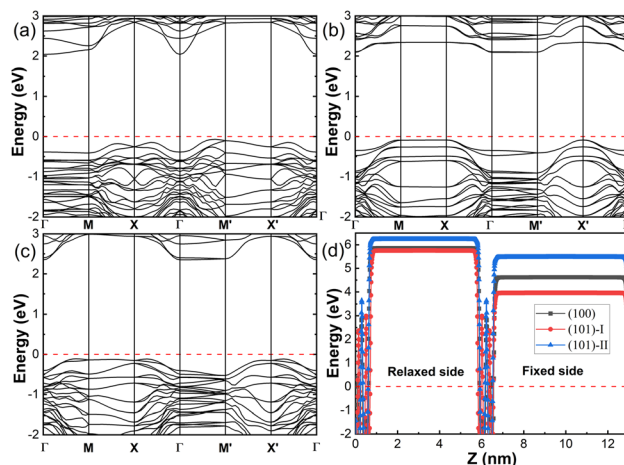| Structure (as labeled in Fig. 1 and S1)	Total energy (eV)	Adsorption energy (eV)
trans-FAZB/(100)	−834.80	−2.68
cis-FAZB/(100)	−834.32	−2.59
trans-FAZB/(101)-I	−826.50	−2.63
cis-FAZB/(101)-I	−825.94	−2.54
trans-FAZB/(101)-II	−835.04	−2.14
cis-FAZB/(101)-II	−834.68	−2.15
PFOS-F/(100)	−839.55	−3.05
PFOS-OH/(100)	−845.91	−3.09
PFOS-F/(101)-I	−832.01	−3.37
PFOS-OH/(101)-I	−838.37	−3.68
PFOS-F/(101)-II	−840.90	−2.73
PFOS-OH/(101)-II	−849.15	−3.16
NO$_3$/(100)	−654.78	−1.08
NO$_3$/(101)-I	−642.26	−2.00
NO$_3$/(101)-II	−652.64	−1.07

Fig. 2 (a–c) Electronic band structure of unbound anatase (100), (101)-I and (101)-II surface along the high-symmetry path, respectively. (d) Potential energy distribution for unbound anatase (100), (101)-I and (101)-II surface. It is plotted along a line perpendicular to the surface. The Fermi energy is set to the valence band maximum (VBM) for comparison.

substrate with a clean surface. According to this definition, exothermic adsorption corresponds to negative values. Table 1 presents the adsorption energies of 12 species of the considered hybrid systems. We found that all the organic adsorbates are chemisorbed on the (100), (101)-I and (101)-II TiO$_2$ surfaces with large adsorption energies. The adsorption energies were at least −2.14 and −2.73 eV for the FAZB- and PFOS-grafted surfaces, respectively, which are much higher than the thermal energy at room temperature (*i.e.*, 0.026 eV), indicating the very stable adsorption of FAZB and PFOS. It is instructive to compare the adsorption energies of organic hybrid systems with inorganic group-grafted anatase surfaces given that the nitrate groups were successfully grafted on a rutile TiO$_2$ surface.[59] We found
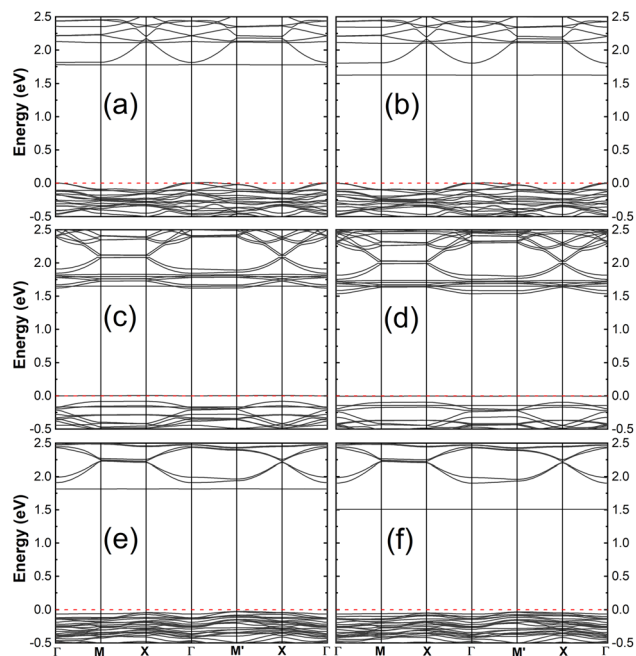
Fig. 3 Electronic band structure of (a) *trans*-FAZB/(100), (b) *cis*-FAZB/(100), (c) *trans*-FAZB/(101)-I, (d) *cis*-FAZB/(101)-I, (e) *trans*-FAZB/(101)-II and (f) *cis*-FAZB/(101)-II. The Fermi energy is set to the valence band maximum (VBM) for comparison.
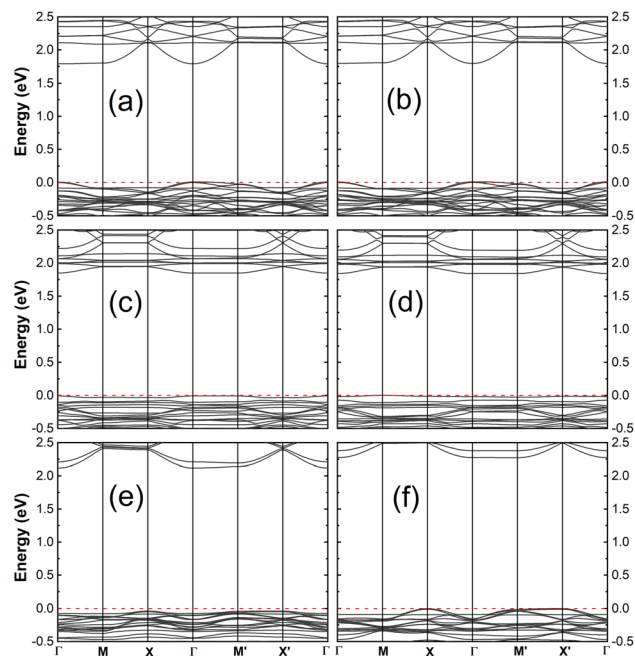

Fig. 4 Electronic band structure of (a) PFOS-F/(100), (b) PFOS-OH/(100), (c) PFOS-F/(101)-I, (d) PFOS-OH/(101)-I, (e) PFOS-F/(101)-II and (f) PFOS-OH/(101)-II. The Fermi energy is set to the valence band maximum (VBM) for comparison.

that the nitrate groups are also chemisorbed on the anatase surfaces stably with adsorption energies slightly smaller than that of the organic hybrid systems.

Given that all the surface properties of the organic/inorganic hybrid systems were derived by truncation of the bulk systems and modification of the initial surfaces, in Fig. S2† and 2 we reported the electronic structures of the TiO_2 bulk and three different pristine anatase surfaces. An indirect band gap of 2.13 eV between the Γ and X points was found for bulk anatase TiO_2, which is significantly smaller than the experimental band

gap value of 3.2 eV (ref. 60) but in agreement with the theoretical studies (2.0 ∼ 2.37 eV).[61,62] Our PBE-computed band gaps for the unbound (100), (101)-I and (101)-II anatase slabs are 2.11, 2.18 and 2.46 eV, respectively, in agreement with the previous studies on TiO_2 slab systems (1.75 ∼ 2.5 eV).[33] Fig. 2(d) shows the typical potential energy distribution across the unbound TiO_2 surface. The vacuum potential at a remote location far away from the surface in the z direction is an asymptotic constant. Given that the valence band maximum was set to zero in our calculation, the vacuum level, which is determined from

Table 2 Energy bandgaps and ionization potentials of the 12 considered hybrid systems

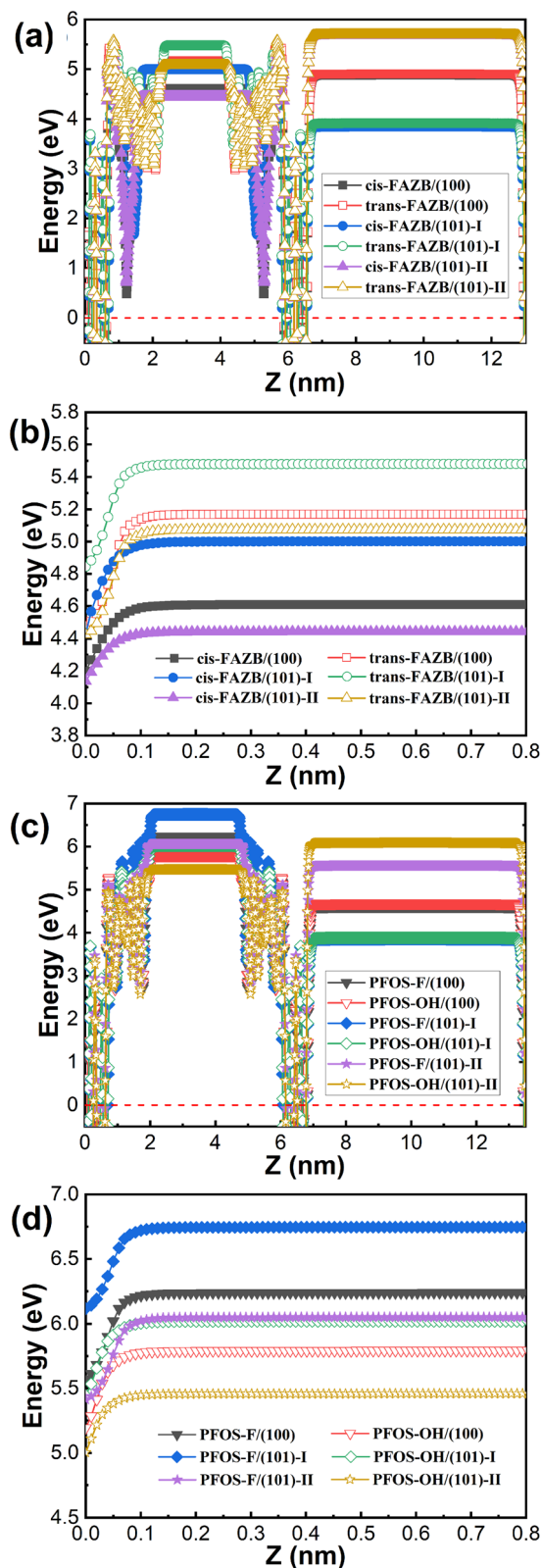| Structure (as labeled in Fig. 1 and S1)	Energy gap (eV)	Ionization potential (eV)	
		Modified side (relaxed side)	Clean side (fixed side)
(100)	2.11	5.86	4.62
(101)-I	2.18	5.76	3.96
(101)-II	2.46	6.23	5.47
trans-FAZB/(100)	1.77	5.17	4.90
cis-FAZB/(100)	1.62	4.61	4.88
trans-FAZB/(101)-I	1.62	5.48	3.92
cis-FAZB/(101)-I	1.54	5.00	3.85
trans-FAZB/(101)-II	1.84	5.07	5.69
cis-FAZB/(101)-II	1.54	4.44	5.68
PFOS-F/(100)	1.78	6.24	4.61
PFOS-OH/(100)	1.79	5.79	4.69
PFOS-F/(101)-I	1.86	6.75	3.85
PFOS-OH/(101)-I	1.84	6.02	3.88
PFOS-F/(101)-II	2.16	6.05	5.55
PFOS-OH/(101)-II	2.27	5.46	6.08

Fig. 5 Potential energies (a) along a line that crosses the adsorbates and is perpendicular to the slab and (b) along the forward path that is perpendicular to the surface with the origin at the outermost atoms of adsorbate for the *cis*-FAZB/(100) (■), *trans*-FAZB/(100) (□), *cis*-FAZB/(101)-I (●), *trans*-FAZB/(101)-I (○), *cis*-FAZB/(101)-II (▲) and *trans*-FAZB/(101)-II (△), (c, d) are the same as (a and b) but for PFOS-F/(100) (▼), PFOS-OH/(100) (▽), PFOS-F/(101)-I (◆), PFOS-OH/(101)-I (◇), PFOS-F/(101)-II (★) and PFOS-OH/(101)-II (☆), respectively.
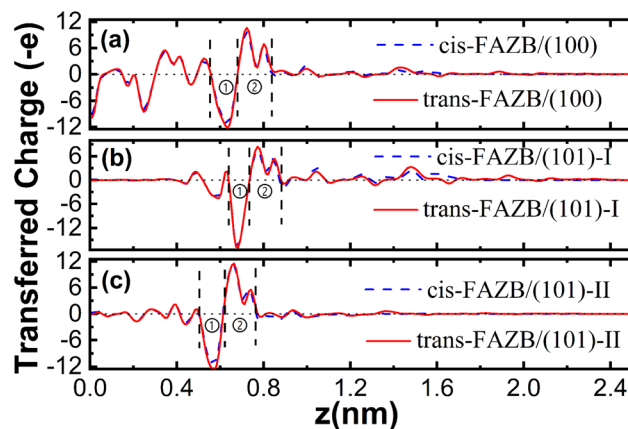
Fig. 6 (a) Linear distribution of transferred electron charge for FAZB-grafted anatase (100) surface. (b and c) Same as (a) but for FAZB-grafted anatase (101)-I and (101)-II surface, respectively. The hybrid system with adsorbate of *trans*-(*cis*-) FAZB is represented with red solid (blue dashed) lines. The vertical dashed lines indicate the encompassing regions of positive (1) and negative charges (2) near the interfaces. The transferred electron charge at the coordinate z is obtained by averaging the transferred electron charge on the corresponding $x–y$ plane.

the electrostatic potential in the vacuum region far enough away from the slab surface, is equal to the ionization potential. For each unbound surface, the difference in ionization potentials between the fixed bottom side and the relaxed top side is influenced by surface relaxation. It is clear that the unbound (101)-II [(101)-I] surface has the highest (lowest) ionization potential.

Here, we consider the impact of adsorption on the electronic structure of the hybrid systems as given by the energy band. The band structures, as depicted in Fig. 3 for the FAZB/TiO$_2$ systems and Fig. 4 for the PFOS/TiO$_2$ systems, show the contribution of the organic adsorbates. For a given TiO$_2$ substrate, all the joint systems are semiconductors with band gaps that are smaller than that of the unbound surface. A comparison of the energy gaps between the hybrid and unbound systems is presented in Table 2, where we notice that for each type of TiO$_2$ substrate, the band gap of the hybrid system with *cis*-FAZB adsorption is smaller than that with *trans*-FAZB adsorption, while the band gaps of the hybrid systems with PFOS-F and PFOS-OH adsorption show small differences.

Given that both the FAZB/TiO$_2$ and PFOS/TiO$_2$ hybrid systems are semiconductors, we explored their ionization potential to quantify the energy barrier to free space that prevents an electron at the valence band maximum from escaping the solid. Fig. 5(a) and (c) show the potential energy distribution of FAZB and PFOS adsorbed on different anatase surfaces, respectively. We plotted the electrostatic potential energy along a line that crosses the adsorbates and is perpendicular to the slab. It is clear that the potential energy in the vicinity of the surface increases gradually as the distance increases for both the adsorbed side and the clean side [Fig. 5(a and c), respectively], but the variation in the potential energy is not monotonous in the former case due to the existence of
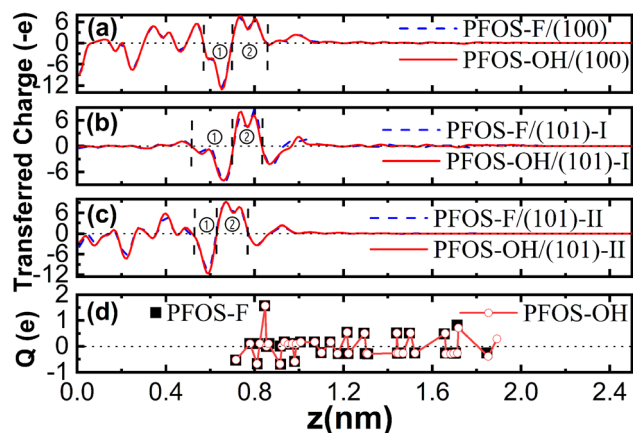
Fig. 7 (a) Linear distribution of transferred electron charge for PFOS-grafted anatase (100) surface. (b and c) Same as (a) but for PFOS-grafted anatase (101)-I and (101)-II surface, respectively. The hybrid system with adsorbate of PFOS-OH (PFOS-F) is represented with red solid (blue dash) lines. The vertical dashed lines indicate the encompassing regions of positive (1) and negative charges (2) near the interfaces. The transferred electron charge at the coordinate z is obtained by averaging the transferred electron charge on the corresponding x–y plane. (d) Mulliken charge distributions on adsorbate of PFOS-OH (○) and PFOS-F (■). The horizontal axis is the coordinate of the atom in the z-direction.
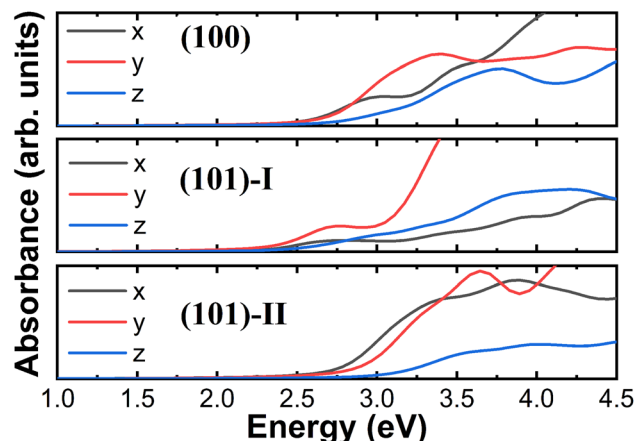

Fig. 8 Absorbance spectra of unbound anatase (100) (top panel), (101)-I (middle) and (101)-II (bottom panel) surface when the polarization direction of incident light is along the x- (black), y- (red) and z (blue)-directions.

adsorbates. We found that the vacuum level of the adsorbed side is different from that of the clean side. The difference in the vacuum levels between the adsorbed side and the clean side is determined by the adsorbate type. It is obvious that the vacuum levels of the clean sides are independent of the type of organic adsorbate on the other side and similar to that of the unbound surfaces without relaxation. To further investigate the potential barriers of the TiO$_2$ surface with different organic switch modifications, we plotted the potential energy curves along the forward path, which is the line perpendicular to the surface, with the origin at the outermost atoms, as shown in Fig. 5(b and d), respectively. The corresponding ionization potentials obtained from the vacuum levels in Fig. 5(b and d) are summarized in Table 2. We noted that the ionization potentials of the FAZB/TiO$_2$ hybrid systems follow the order of *trans*-FAZB/(101)-I > *trans*-FAZB/(100) > *trans*-FAZB/(101)-II > *cis*-FAZB/(101)-I > *cis*-FAZB/(100) > *cis*-FAZB/(101)-II. We found that the adsorption on a semiconducting substrate with each given FAZB configuration changes the relative order of the ionization potential between the different TiO$_2$ surfaces compared to that without adsorption. For example, the relative order of the ionization potential for the (100), (101)-I and (101)-II hybrid surfaces grafted with *trans*-FAZB is different from that for the (100), (101)-I and (101)-II unbound surfaces. Clearly, regardless of the type of anatase surface, the ionization potential of the TiO$_2$ surface grafted with *trans*-FAZB is always larger than that with *cis*-FAZB. Alternatively, the ionization potential of the TiO$_2$ surface modified with various short carbon chain silanes follows the order of PFOS-F/(101)-I > PFOS-F/(100) > PFOS-F/(101)-II > PFOS-OH/(101)-I > PFOS-OH/(100) > PFOS-OH/(101)-II. It is clear that ionization potentials of the different types of TiO$_2$ surfaces modified with

a given silane exhibit the same relative order as that of the TiO$_2$ surfaces modified with a given FAZB. The PFOS-F-grafted TiO$_2$ surface also shows a larger ionization potential than the PFOS-OH-grafted TiO$_2$ surface. Notably, the hierarchy of the ionization potential of the hybrid systems predicted by our numerical calculations was found to follow the same trend of hydrophobicity in experimental measurements [105° (23°) contact angle for the *trans*-state (*cis* state) FAZB-grafted silica-encapsulated nanoparticles[23] and 165° (<10°) contact angle for PFOS-F (PFOS-OH)-grafted TiO$_2$ nanoparticles[25]], which can be explained by the induced polar interaction model at the liquid/solid interfaces.[44] When a polar liquid (*e.g.*, water) is in contact with a polarizable solid surface, the induced solid/liquid polar interaction, and thereby the surface hydrophilicity increases with the solid surface polarizability monotonously, which is inversely related to the ionization potential.[41–43] Thus, we can expect that the equilibrium contact angle for contacting a polar liquid will increase with an increase in the ionization potential of solid surface, *i.e.*, the surface hydrophobicity of *trans*-FAZB (PFOS-F)-grafted TiO$_2$ is larger than that of *cis*-FAZB (PFOS-OH)-grafted TiO$_2$.

To understand how the organic adsorbates affect the surface potential, we considered in detail the redistributions of the electron charges between the inorganic substrate and the organic adsorbate, as shown in Fig. 6 and 7. A common feature is that the charge redistributions are locally confined in the vicinity of the interface between the TiO$_2$ surface and the adsorbates. In the case of the FAZB/TiO$_2$ (PFOS/TiO$_2$) hybrid system, the positive charges accumulate on the top layer of the TiO$_2$ substrate [indicated in Fig. 6 (Fig. 7)], while negative charges accumulate at the binding site of FAZB (PFOS) [indicated in Fig. 6 (Fig. 7)]. However, the end-to-end distance and the linear distribution of transferred electron charge for the planar rod-like *trans*-FAZB is larger than that of nonplanar *cis*-FAZB, suggesting that the *trans*-FAZB receives more electrons from the interface and induces a larger dipole moment whose direction points inwards from the TiO$_2$ substrate. It had been
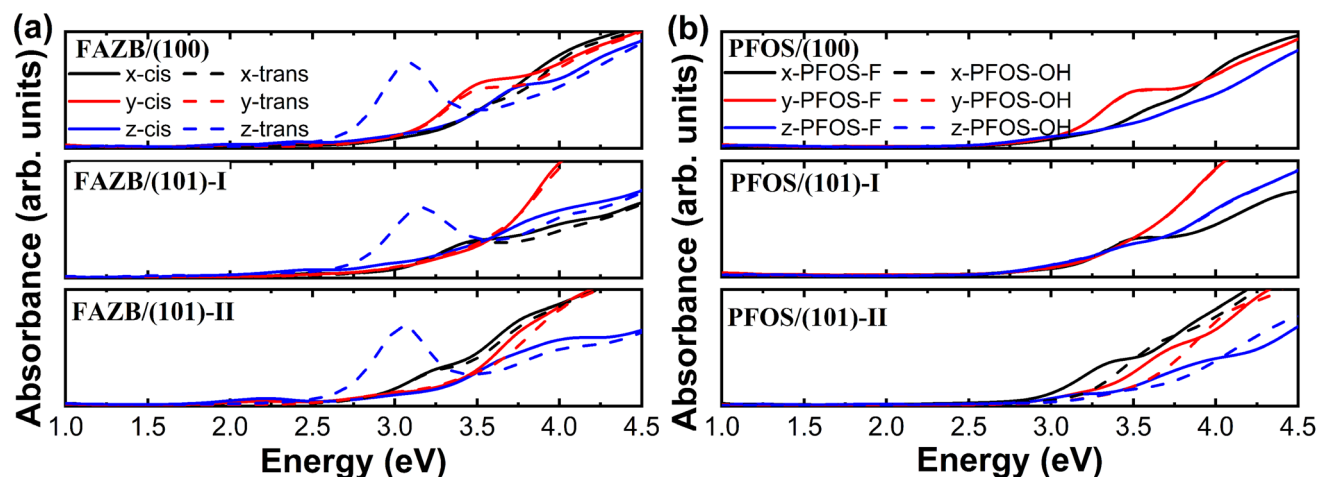
Fig. 9 (a) Absorbance spectra of *cis*-FAZB- (solid) and *trans*-FAZB (dash)-grafted anatase (100) (top panel), (101)-I (middle) and (101)-II (bottom panel) surface when the polarization direction is along the *x*- (black), *y*- (red) and *z* (blue)-directions. (b) Absorbance spectra of PFOS-F (solid)- and PFOS-OH (dash)-grafted anatase (100) (top panel), (101)-I (middle) and (101)-II (bottom panel) surface when the polarization direction of incident light is along the *x*- (black), *y*- (red) and *z* (blue)-directions. The scissors operation of 0.66 eV is applied.

reported that the adsorbate on the substrate reduces (enhances) the electron binding capability, *i.e.*, work function or ionization potential, by forming a plane of dipoles, whose direction points outwards (inwards) from the substrate.[37] Therefore, compared to the case of the *cis*-FAZB-grafted TiO_2 surface, the higher ionization potential for the *trans*-FAZB-grafted TiO_2 surface can be attributed to the larger electron charge transfer caused by chemical functionalization and structural relaxation effect. Alternatively, the relative order of ionization potential between the PFOS-F- and PFOS-OH-grafted TiO_2 surfaces cannot be explained by the effect of the induced dipole moment derived from charge transfer only. As shown in Fig. 7, for a given TiO_2 surface, the linear distribution of transferred electron charge of PFOS with hydroxyl substitution is almost the same as that of pristine PFOS. It is widely known that the hydroxyl group is a polar chemical group with an intrinsic dipole moment pointing from oxygen to hydrogen. Fig. 7(d) shows the dipole moment contributions of the PFOS-F and PFOS-OH adsorbates. The contribution of the OH dipole moment to the potential barrier is negative given that its direction points outwards to the anatase slab [Fig. 7(d)]. This explains why the OH-substituted PFOS exhibits exceptionally low ionization potentials. The effect of the intrinsic dipole moments of the functional groups was also predicted with an increase or decrease in the potential barriers of several surfaces.[46,63]

Also, we calculated the UV-vis absorbance spectra of the hybrid organic/inorganic systems to probe the grafting-induced changes in their optical properties. Consequently, a significant anisotropic absorbance was found for the bare and hybrid surfaces. The first absorption bands in Fig. 8 are 3.02, 2.74 and 3.39 eV for the (100), (101)-I and (101)-II unbound TiO_2 surfaces, respectively. Our computed first absorption band of the (101)-I unbound surface is consistent with other theoretical calculations (2.56 eV)[34] but is underestimated compared with the experimental measurements, which is located between 3.4 and

4.9 eV performed on TiO_2 films with different thicknesses.[64] To obtain the exact optical properties in the UV-vis range, the scissors operation[65] of 0.66 eV, which corresponds to the difference between the experimental measurement of the thinnest TiO_2 films ($\sim$15 nm) considered in a previous study and our theoretical result, was carried out in an optical absorbance of the hybrid system. As shown in Fig. 9(a), we found that the absorbance spectra of the TiO_2 surface grafted with *trans*-FAZB are slightly different from that with *cis*-FAZB, except for the case of TiO_2 surface grafted with *trans*-FAZB in the *z* polarization direction, which exhibits an additional absorption peak at about 3.2 eV, corresponding to the conformational switch of azobenzene-containing units from the apparent wetting state (*i.e.*, *trans* isomer) to the fully wetting state (*i.e.*, *cis* isomer) under UV irradiation.[23] In addition, the absorbance spectra of the (101)-II TiO_2 surface grafted with PFOS-F are also slightly different from that with PFOS-OH [Fig. 9(b)], while the absorbance spectra of PFOS-F- and PFOS-OH-grafted TiO_2 surfaces are similar for the (100) and (101)-I surfaces. The absorption peak at about 3.6 eV for the PFOS-grafted TiO_2 surface can be assigned to the oxidization of PFOS upon UV illumination.[25]

4 Conclusions

Density functional theory calculations were performed on hybrid systems containing organic switches adsorbed on low-index TiO_2 anatase surfaces. We considered the *trans*-FAZB and *cis*-FAZB isomers anchored by carboxyl groups on one side of the isomer, while the pristine PFOS-F and oxidized PFOS-OH bonded by the oxygen atoms in the siloxane groups. The reliability of our models was demonstrated by examining the chemically intuitive parameter, *i.e.*, adsorption energies. To understand how the different conformations of the organic switches interact with the inorganic surface, we investigated their electronic structures and surface potentials and analyzed their charge redistributions. The band gaps of the hybrid

systems are reduced upon adsorption. For each type of TiO$_2$ surface, while the *trans*-FAZB-grafted TiO$_2$ surface exhibits a larger band gap than the *cis*-FAZB-grafted TiO$_2$ surface, both the PFOS-F- and PFOS-OH-grafted TiO$_2$ surfaces have similar band gaps. The effect of organic switch modifications was found to be crucial to determine the relative order of the ionization potentials among the different TiO$_2$ surfaces. Moreover, we systematically studied the organic switch configuration dependence of the ionization potentials of the functionalized TiO$_2$ surfaces with FAZB and PFOS adsorbates and found that regardless of the type of TiO$_2$ surface, the *cis*-FAZB (PFOS-OH)-grafted TiO$_2$ exhibits a lower ionization potential than the *trans*-FAZB (PFOS-F)-grafted TiO$_2$. By considering the two important factors in tuning the surface dipole moments, as follows: (i) the electron charge redistribution at the interface caused by chemical functionalization and structural relaxation effect and (ii) the polarity of attached chemical groups, we successfully explained the different behaviors of the ionization potentials for the *trans*-/*cis*-FAZB- and PFOS-F/PFOS-OH-terminated TiO$_2$ surfaces. By combining the induced polar interaction analysis and the experimental measurements in the literature, we demonstrated that the ionization potential is an important predictor of the surface wetting properties of the adsorbed systems. Anisotropic absorbance for the considered hybrid surfaces was also found. The first absorption peak of TiO$_2$ grafted with *trans*-FAZB (PFOS-F) was assigned to the conformational switch (oxidization) under UV irradiation. This study represents the first effort to rationalize the surface potentials of organic/inorganic systems *via* first-principles modeling, which can be helpful for the proper design and selection of organic coatings with controllable surface properties for photosensitive material applications, such as chemical sensors, artificial intelligent surfaces, and microfluidic devices.

Author contributions

Haiming Huang: conceptualization, methodology, validation, investigation, formal analysis, visualization, writing – review & editing. Mingquan Ding, Yu Zhang, Shuai Zhang and Yiyun Ling: investigation, formal analysis, visualization. Weiliang Wang: methodology, validation, supervision, project administration, writing – review & editing. Shaolin Zhang: conceptualization, supervision, project administration, writing – review & editing.

Conflicts of interest

There are no conflicts to declare.

Acknowledgements

References

1 Y. B. Zheng, B. K. Pathem, J. N. Hohman, J. C. Thomas, M. Kim and P. S. Weiss, *Adv. Mater.*, 2013, **25**, 302–312.
2 M. M. Russew and S. Hecht, *Adv. Mater.*, 2010, **22**, 3348–3360.
3 S. L. Oscurato, M. Salvatore, P. Maddalena and A. Ambrosio, *Nanophotonics*, 2018, **7**, 1387–1422.
4 E. Pantuso, G. De Filpo and F. P. Nicoletta, *Adv. Opt. Mater.*, 2019, **7**, 1900252.
5 V. Y. Chang, C. Fedele, A. Priimagi, A. Shishido and C. J. Barrett, *Adv. Opt. Mater.*, 2019, **7**, 1900091.
6 S. L. Oscurato, F. Borbone, P. Maddalena and A. Ambrosio, *ACS Appl. Mater. Interfaces*, 2017, **9**, 30133–30142.
7 B. Ziolkowski, M. Czugala and D. Diamond, *J. Intell. Mater. Syst. Struct.*, 2013, **24**, 2221–2238.
8 H. M. D. Bandara and S. C. Burdette, *Chem. Soc. Rev.*, 2012, **41**, 1809–1825.
9 L. Zhang and J. M. Cole, *ACS Appl. Mater. Interfaces*, 2014, **6**, 3742–3749.
10 M. Irie, *Chem. Rev.*, 2000, **100**, 1685–1716.
11 R. Klajn, *Chem. Soc. Rev.*, 2014, **43**, 148–184.
12 X. J. Feng, L. Feng, M. H. Jin, J. Zhai, L. Jiang and D. B. Zhu, *J. Am. Chem. Soc.*, 2004, **126**, 62–63.
13 Q. T. H. Ta, S. Park and J. S. Noh, *J. Colloid Interface Sci.*, 2017, **505**, 437–444.
14 M. Hilal and W. Yang, *Nano Convergence*, 2022, **9**, 14.
15 S. T. Wang, X. J. Feng, J. N. Yao and L. Jiang, *Angew. Chem., Int. Ed.*, 2006, **45**, 1264–1267.
16 D. S. Kommireddy, A. A. Patel, T. G. Shutava, D. K. Mills and Y. M. Lvov, *J. Nanosci. Nanotechnol.*, 2005, **5**, 1081–1087.
17 X. J. Xie and E. Bakker, *J. Am. Chem. Soc.*, 2014, **136**, 7857–7860.
18 Q. Q. Ding, R. Li, M. D. Chen and M. T. Sun, *Appl. Mater. Today*, 2017, **9**, 251–258.
19 D. P. Hoffman, O. P. Lee, J. E. Millstone, M. S. Chen, T. A. Su, M. Creelman, J. M. J. Frechet and R. A. Mathies, *J. Phys. Chem. C*, 2013, **117**, 6990–6997.
20 M. Zuleta, T. Edvinsson, S. Yu, S. Ahmadi, G. Boschloo, M. Gothelid and A. Hagfeldt, *Phys. Chem. Chem. Phys.*, 2012, **14**, 10780–10788.
21 Y. P. Zhang, Y. S. Wang, Z. Q. Xu, J. Y. Liu, J. C. Song, Y. Z. Xue, Z. Y. Wang, J. L. Zheng, L. C. Jiang, C. X. Zheng, F. Z. Huang, B. Q. Sun, Y. B. Cheng and Q. L. Bao, *ACS Nano*, 2016, **10**, 7031–7038.
22 S. B. Ma, H. K. Ting, Y. Z. Ma, L. L. Zheng, M. W. Zhang, L. X. Xiao and Z. J. Chen, *AIP Adv.*, 2015, **5**, 057154.
23 S. Pan, R. Guo and W. Xu, *Soft Matter*, 2014, **10**, 9187–9192.
24 Y. Ito, M. Heydari, A. Hashimoto, T. Konno, A. Hirasawa, S. Hori, K. Kurita and A. Nakajima, *Langmuir*, 2007, **23**, 1845–1850.

25 Y. Pan, W. Kong, B. Bhushan and X. Zhao, *Beilstein J. Nanotechnol.*, 2019, **10**, 866–873.

26 J. W. Zhao, L. Xue, Z. J. Niu, L. Huang, Y. D. Hou, Z. Z. Zhang, R. S. Yuan, Z. X. Ding, X. Z. Fu, X. Lu and J. L. Long, *J. Power Sources*, 2021, **512**, 230532.

27 J. W. Zhao, L. Huang, L. Xue, Z. J. Niu, Z. Z. Zhang, Z. X. Ding, R. S. Yuan, X. Lu and J. L. Long, *J. Energy Chem.*, 2023, **79**, 601–610.

28 J. W. Zhao, B. Q. Liu, L. S. Meng, S. He, R. S. Yuan, Y. D. Hou, Z. X. Ding, H. X. Lin, Z. Z. Zhang, X. X. Wang and J. L. Long, *Appl. Catal., B*, 2019, **256**, 117823.

29 H. W. Zhang, P. Zhang, J. W. Zhao, Y. Liu, Y. Huang, H. W. Huang, C. Yang, Y. B. Zhao, K. F. Wu, X. L. Fu, S. Y. Jin, Y. D. Hou, Z. X. Ding, R. S. Yuan, M. B. J. Roeffaers, S. C. Zhong and J. L. Long, *Angew. Chem., Int. Ed.*, 2021, **60**, 16009–16018.

30 P. Zhang, X. Y. Sui, Y. Wang, Z. Wang, J. W. Zhao, N. Wen, H. L. Chen, H. W. Huang, Z. Z. Zhang, R. S. Yuan, Z. X. Ding, W. X. Dai, X. Z. Fu, Y. X. Weng and J. L. Long, *J. Am. Chem. Soc.*, 2023, **145**, 5769–5777.

31 L. Dworak, M. Zastrow, G. Zeyat, K. Ruck-Braun and J. Wachtveitl, *J. Phys.: Condens. Matter*, 2012, **24**, 394007.

32 P. Bluemmel, A. Setaro, C. Maity, S. Hecht and S. Reich, *J. Phys.: Condens. Matter*, 2012, **24**, 394005.

33 K. J. Chen, A. Charaf-Eddin, B. Selvam, F. Boucher, A. D. Laurent and D. Jacquemin, *J. Phys. Chem. C*, 2015, **119**, 3684–3696.

34 A. Belhboub, F. Boucher and D. Jacquemin, *J. Phys. Chem. C*, 2016, **120**, 18281–18288.

35 K. J. Chen, F. Boucher and D. Jacquemin, *J. Phys. Chem. C*, 2015, **119**, 16860–16869.

36 Z. Deng, Z. Li and W. Wang, *Chem. Phys. Lett.*, 2015, **637**, 26–31.

37 W. Wang and Z. Li, *J. Appl. Phys.*, 2011, **109**, 114308.

38 C. Q. Sun, *Nano Mater. Sci.*, 2020, **2**, 333–345.

39 J. L. Freeouf and J. M. Woodall, *Appl. Phys. Lett.*, 1981, **39**, 727.

40 Y. Ando, Y. Gohda and S. Tsuneyuki, *Surf. Sci.*, 2012, **606**, 1501–1506.

41 I. K. Dmitrieva and G. I. Plindov, *Phys. Scr.*, 1983, **27**, 402–406.

42 K. R. S. Chandrakumar, T. K. Ghanty and S. K. Ghosh, *J. Phys. Chem. A*, 2004, **108**, 6661–6666.

43 P. Politzer, P. Jin and J. S. Murray, *J. Chem. Phys.*, 2002, **117**, 8197–8202.

44 A. Carre, *J. Adhes. Sci. Technol.*, 2007, **21**, 961–981.

45 H. Huang, W. Wang and L. Wang, *Phys. Chem. Chem. Phys.*, 2019, **21**, 8257–8263.

46 M. Khazaei, M. Arai, T. Sasaki, A. Ranjbar, Y. Y. Liang and S. Yunoki, *Phys. Rev. B: Condens. Matter Mater. Phys.*, 2015, **92**, 075411.

47 W. Li, L. G. C. Rego, F. Q. Bai, C. P. Kong and H. X. Zhang, *RSC Adv.*, 2014, **4**, 19690–19693.

48 F. De Angelis, S. Fantacci and R. Gebauer, *J. Phys. Chem. Lett.*, 2011, **2**, 813–817.

49 A. G. Thomas and K. L. Syres, *Chem. Soc. Rev.*, 2012, **41**, 4207–4217.

50 G. Pilania, K. Slenes and R. Ramprasad, *J. Appl. Phys.*, 2013, **113**, 064316.

51 A. Y. Fadeev and T. J. McCarthy, *J. Am. Chem. Soc.*, 1999, **121**, 12184–12185.

52 F. Labat, P. Baranek and C. Adamo, *J. Chem. Theory Comput.*, 2008, **4**, 341–352.

53 J. P. Perdew, K. Burke and M. Ernzerhof, *Phys. Rev. Lett.*, 1996, **77**, 3865–3868.

54 G. Kresse and J. Furthmuller, *Phys. Rev. B: Condens. Matter Mater. Phys.*, 1996, **54**, 11169–11186.

55 G. Kresse and J. Furthmuller, *Comput. Mater. Sci.*, 1996, **6**, 15–50.

56 G. Kresse and D. Joubert, *Phys. Rev. B: Condens. Matter Mater. Phys.*, 1999, **59**, 1758–1775.

57 H. J. Monkhorst and J. D. Pack, *Phys. Rev. B: Solid State*, 1976, **13**, 5188–5192.

58 S. C. Li, Y. Losovyj, V. K. Paliwal and U. Diebold, *J. Phys. Chem. C*, 2011, **115**, 10173–10179.

59 H. Wang, X. T. Hu, Y. J. Ma, D. J. Zhu, T. Li and J. Y. Wang, *Chin. J. Catal.*, 2020, **41**, 95–102.

60 S. P. Kowalczyk, F. R. McFeely, L. Ley, V. T. Gritsyna and D. A. Shirley, *Solid State Commun.*, 1977, **23**, 161–169.

61 R. Asahi, Y. Taga, W. Mannstadt and A. J. Freeman, *Phys. Rev. B: Condens. Matter Mater. Phys.*, 2000, **61**, 7459–7465.

62 S. Mo and W. Y. Ching, *Phys. Rev. B: Condens. Matter Mater. Phys.*, 1995, **51**, 13023–13032.

63 P. C. Rusu and G. Brocks, *J. Phys. Chem. B*, 2006, **110**, 22628–22634.

64 A. Mills, G. Hill, S. Bhopal, I. P. Parkin and S. A. O'Neill, *Phys. Rev. B: Condens. Matter Mater. Phys.*, 2003, **160**, 185–194.

65 M. R. Pederson and B. M. Klein, *Phys. Rev. B: Condens. Matter Mater. Phys.*, 1988, **37**, 10319–10331.